

## IONTRONICS

# Microscale droplet assembly enables biocompatible multifunctional modular iontronics

Yujia Zhang<sup>1,2\*</sup>, Cheryl M. J. Tan<sup>3,4</sup>, Christopher N. Toepfer<sup>4</sup>, Xin Lu<sup>3</sup>, Hagan Bayley<sup>1\*</sup>

Hydrogel iontronic devices can emulate biological functions and communicate with living matter. But the fabrication of miniature, soft iontronic devices according to modular designs has not been achieved. In this work, we report the use of surfactant-supported assembly of freestanding microscale hydrogel droplets to construct various iontronic modules, circuits, and biointerfaces. Chemical modifications of silk fibroin produced a pair of oppositely charged hydrogels. Microscale assembly of various combinations of hydrogel droplets produced iontronic diodes, npn- and pnp-type transistors, and diverse reconfigurable logic gates. Through the incorporation of poly(amino acid)s, we have demonstrated a droplet-based synthetic synapse with ionic polymer-mediated long-term plasticity. Further, our iontronic transistor can serve as a biocompatible sensor to record electrophysiological signals from sheets of human cardiomyocytes, paving a way to the building of miniature bioiontronic systems.

The field of iontronics is rapidly expanding because of its promising applications in abiotic-biotic interfaces (1–3), energy-storage devices (4–7), neuroprosthetics (8–11), and neuromorphic computing (12–16). Hydrogel-based iontronic devices have been extensively studied owing to their high ion conductivity, intrinsic softness, and biocompatibility (17). Iontronic devices, including diodes (18–20), transistors (21–24), and functional circuits (25–27), have been fabricated by using charge-selective hydrogels to mimic the behavior of p- and n-type semiconductors. However, the hydrogel-based iontronic devices produced so far are mainly based on micro- or nanofluidic systems with electrolytes confined within solid channels (28). The large volume occupied by rigid scaffolds for fluidics and the complex fabrication procedures of solid-state devices hinder their use as iontronic modules. The reliance on solid-state devices also limits the possibility of integration with soft tissues.

Devices made from nanoliter hydrogel droplets hold potential for use in the production of miniature, soft iontronic components that are not tethered to fluidic channels (i.e., are freestanding) and can function at abiotic-biotic interfaces. For example, ionic current modulation of neuronal activity can be achieved by directly interfacing droplet-based power sources with living neural microtissues and mouse brain slices (7). Despite its importance, in the realm of iontronics, effective control of ion transport and signal processing in droplet-based systems has not yet emerged.

In this work, we report a set of freestanding, microscale, soft iontronic modules, termed droplettronics, which are made through the self-assembly of surfactant-supported, nanoliter, silk hydrogel droplets. Protein modifications produced cation- and anion-selective silk hydrogels, in which either anions or cations were fixed to the silk fibroins that retained mobile counterions, making them ionic analogs of p- and n-type semiconductors (Fig. 1A). By configuring combinations of droplets, droplettronics could be used to produce droplet-based diodes, transistors, various reconfigurable logic gates, and synthetic synapses with ionic polymer-mediated long-term plasticity. Further, a droplettronic device could interface with sheets of cardiomyocytes and detect electrical signals from them.

## Design and fabrication of droplettronics

We prepared the cation-selective pregel solution by mixing a silk fibroin solution with a hyaluronic acid–tyramine conjugate (Fig. 1B). The anion-selective pregel solution was obtained through carbodiimide coupling of silk fibroin with poly-L-lysine and 1,3-dimethylimidazolium-2-carboxylate, following procedures documented in the literature (see materials and methods) (29). The modified silk pregels showed altered ultraviolet (UV)–visible absorbance spectra (Fig. 1C). Zeta potential measurements reflected the charge selectivities of the modified silk pregels: native silk, –22.5 mV; cation-selective silk, –47 mV; and anion-selective silk, +41 mV (Fig. 1D) (30).

We used surfactant-supported assembly of hydrogel droplets to construct various droplettronic devices (Fig. 1, E and F, and supplementary text) (7). In brief, the pregel droplets were deposited in a surfactant-containing oil with a microinjector. The droplets formed interface bilayers (DIBs) within seconds after contact with one another. The DIBs allowed the fabrication of hydrogel assemblies with distinct

compartments. Our approach produced droplets as small as 0.5 nL, which are less than 100 μm in diameter. After assembly, UV irradiation for 1 min initiated photochemical dityrosine cross-linking of the silk hydrogel (31, 32), which ruptured the DIBs, with the constituent surfactants diffusing into the oil phase (fig. S1). The rupture process established ion conductive pathways, thereby activating the droplettronic devices. Only counterions were mobile in the devices owing to Donnan exclusion, which mimicked the behaviors of charge carriers in p- and n-type semiconductors. The primary mobile counterions were sodium ions in the cation-selective hydrogel and chloride ions in the anion-selective hydrogel (see materials and methods). By combining droplets of cation- and anion-selective hydrogels into doublets and triplets, modular droplettronic diodes and transistors were produced (Fig. 1G and fig. S2).

## Droplettronic diodes

We characterized ionic rectification of the droplettronic diode by using platinum electrodes to apply a voltage scan (Fig. 2A). The current (*I*)–voltage (*V*) curves were asymmetric, with higher conduction under the forward bias, that is, from the cation-selective hydrogel to the anion-selective hydrogel (Fig. 2B). The result is consistent with a model of bipolar membrane heterojunctions (23), which leads to mobile ion accumulation and high ionic conductivity under forward bias as well as ion depletion and low ionic conductivity under reverse bias. The impedance of our droplettronic diode under a forward bias was around 3000 times lower than that under a reversed bias (fig. S3). The impedance differential was maintained at scan frequencies below 100 Hz and decreased under higher frequencies on account of the ion hysteresis effect, which was caused by the delay of ion migration in and out of the heterojunction. The Bode phase plot and the Nyquist plot of a droplettronic diode under a forward bias were also consistent with the heterojunction model and equivalent circuit response (23).

Device miniaturization, which might benefit device performance but is demanding to achieve, has been a long-standing pursuit for hydrogel-based iontronics (21, 25). The use of surfactant-supported hydrogel droplets to build droplettronics facilitates miniaturization. Further, we found an increased rectification ratio (the ratio between forward and reverse bias currents) when we decreased the droplet volume. Decreasing the volume of the droplets from 50 to 0.5 nL produced an increase in the rectification ratio from  $I_{+1.5V}/I_{-1.5V} \approx 6$  and  $I_{+4V}/I_{-4V} \approx 21$  to 97 and 215, respectively, and a decrease in peak current (from 31 to 2.8 μA at +4 V; fig. S4). The changes were attributed to an increase in the volume ratio of the ionic heterojunction with respect to

<sup>1</sup>Department of Chemistry, University of Oxford, Oxford, UK.

<sup>2</sup>Institute of Electrical and Microengineering, École Polytechnique Fédérale de Lausanne, Lausanne, Switzerland.

<sup>3</sup>Ludwig Institute for Cancer Research, Nuffield Department of Medicine, University of Oxford, Oxford, UK. <sup>4</sup>Division of Cardiovascular Medicine, Radcliffe Department of Medicine, University of Oxford, Oxford, UK.

\*Corresponding author. Email: yujia.zhang@epfl.ch (Y.Z.); hagan.bayley@chem.ox.ac.uk (H.B.)

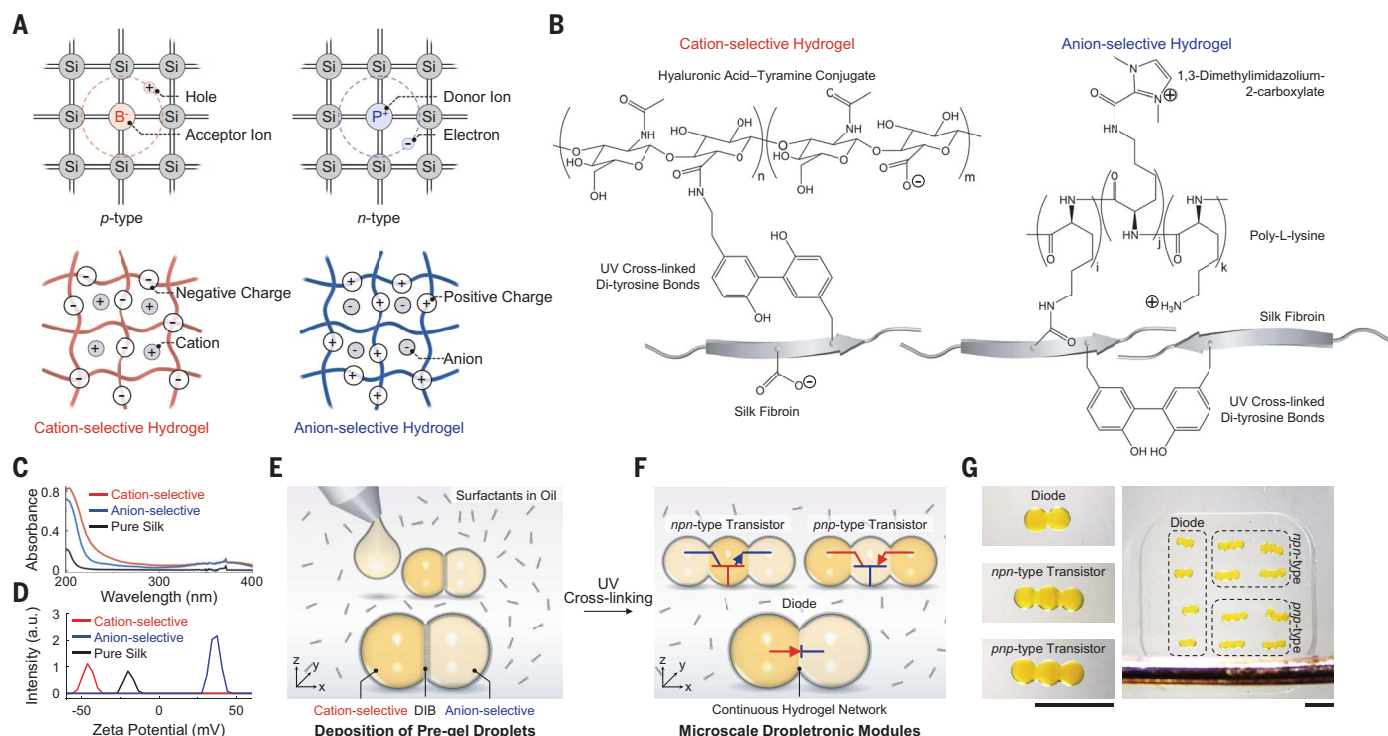


**Fig. 1. Formation of droplettronic devices with two oppositely charged silk hydrogels.** (A) Cation- and anion-selective hydrogels are the ionic equivalents of p- and n-type electronic semiconductors. (B) Chemical structures of the cation- and anion-selective silk hydrogels. (C) UV-visible absorbance spectra of silk fibroin before and after modifications. (D) Zeta potentials of silk fibroin before and after modifications. (E) Fabrication of droplettronic devices through the consecutive deposition of hydrogel droplets. Silk pregel

droplets were submerged in a surfactant-containing oil and acquired surfactant monolayer coatings, which formed DIBs when droplets were placed in contact with each other. (F) The modules were activated by UV cross-linking of the silk hydrogel, which ruptured the insulating DIBs to form continuous hydrogel structures. (G) Bright-field images of a droplettronic diode and transistors (left) and multiple modules compared with a platinum electrode with diameter of 250  $\mu\text{m}$  (right). Droplet volume is 0.5 nl. Scale bars are 250  $\mu\text{m}$ .

volumes of the droplets and the increased internal resistance of the droplets (supplementary text). Droplettronic diodes also showed fast responses under an alternating bias (Fig. 2C), for example,  $0.2 \pm 0.1$  and  $0.7 \pm 0.3$  s rise or fall times for 0.5 and 10 nl droplets, respectively. The rectification performance was superior to that of reported macroscale, soft iontronic diodes and comparable to that of the best of solid-state iontronic diodes (table S1). Water in hydrogels tended to evaporate over time and inactivate droplettronic devices (Fig. 2C and fig. S5). Nevertheless, the droplets could be rehydrated and the devices reactivated by soaking them with water applied to the surface. Droplettronics could also be preserved in humid environments, such as on a water-saturated silica gel substrate (fig. S6). The two approaches can extend the operation time of droplettronics to more than 24 hours.

### Droplettronic transistors and logic circuits

We next constructed an npn-type droplettronic bipolar junction transistor (Fig. 3A), in which two terminal droplets served as the collector (C) and emitter (E) and a central droplet served as the base (B). The current  $I_{\text{BE}}$  regulated

collector-emitter anion transport ( $I_{\text{CE}}$ ) by pushing mobile cations into the C/B and B/E interfaces or pulling them away. When  $I_{\text{BE}} \leq 0$   $\mu\text{A}$ , the ion depletion was enhanced at the droplet interfaces, leading to a small  $I_{\text{CE}}$  during a sweep of  $V_{\text{CE}}$  with low energy dissipation in the nanowatt range (Fig. 3B). In comparison, a positive  $I_{\text{BE}}$  activated anion transport and enabled transistor operation, showing three operation regions similar to an electronic bipolar junction transistor; that is, saturation, active, and breakdown regions. The  $I_{\text{CE}}-V_{\text{CE}}$  curves can be described by extension of the classical model of bipolar junction transistors (33), and the breakdown is likely ascribed to electrolysis of water at high  $V_{\text{CE}}$ . By switching the positions of the cation- and anion-selective hydrogels, a pnp-type droplettronic transistor was also constructed, which showed transistor characteristics based on cation transport (fig. S7).

We further investigated the transistor operation by recording  $I_{\text{CE}}$  under a fixed  $V_{\text{CE}}$  by sweeping the  $I_{\text{BE}}$  input (Fig. 3C). The current ratio between the on ( $I_{\text{BE}} = 1$   $\mu\text{A}$ ) and off ( $I_{\text{BE}} \leq 0$   $\mu\text{A}$ ) states was around 80, which is superior to that of reported macroscale iontronic transistors (table S2). An ionic amplification gain

( $g = I_{\text{CE}}/I_{\text{BE}}$ ) of around 2 was obtained at  $V_{\text{CE}} = 2$  V (fig. S8), which is of the same order of magnitude as that of previous iontronic transistors. When operating in the active region, the energy consumption was in the microwatt range and no pronounced performance change was observed over time, when water evaporation was minimized (Fig. 3D). Transistors made from 0.5-nl droplets showed a fast response under an alternating input (Fig. 3E), resulting in a rise time of  $0.7 \pm 0.1$  s and a fall time of  $0.4 \pm 0.1$  s (fig. S9). The on-off ratio and the switching characteristics were maintained at alternating frequencies of  $I_{\text{BE}}$  below 10 Hz (fig. S10), demonstrating the possibility of processing ionic signals with transients of around 0.1 s.

To enable practical ion-based computation, such as logic operations, it is essential to connect multiple iontronic devices. The droplettronic modules can be connected by hydrophilic attraction in a surfactant-free oil and disassembled to form other connections, which allowed us to assemble a set of logic gates by reconfiguring two NOT gates as building modules. A NOT gate comprised an npn-type droplettronic transistor in serial connection with a resistor droplet of native silk hydrogel (Fig. 3F),

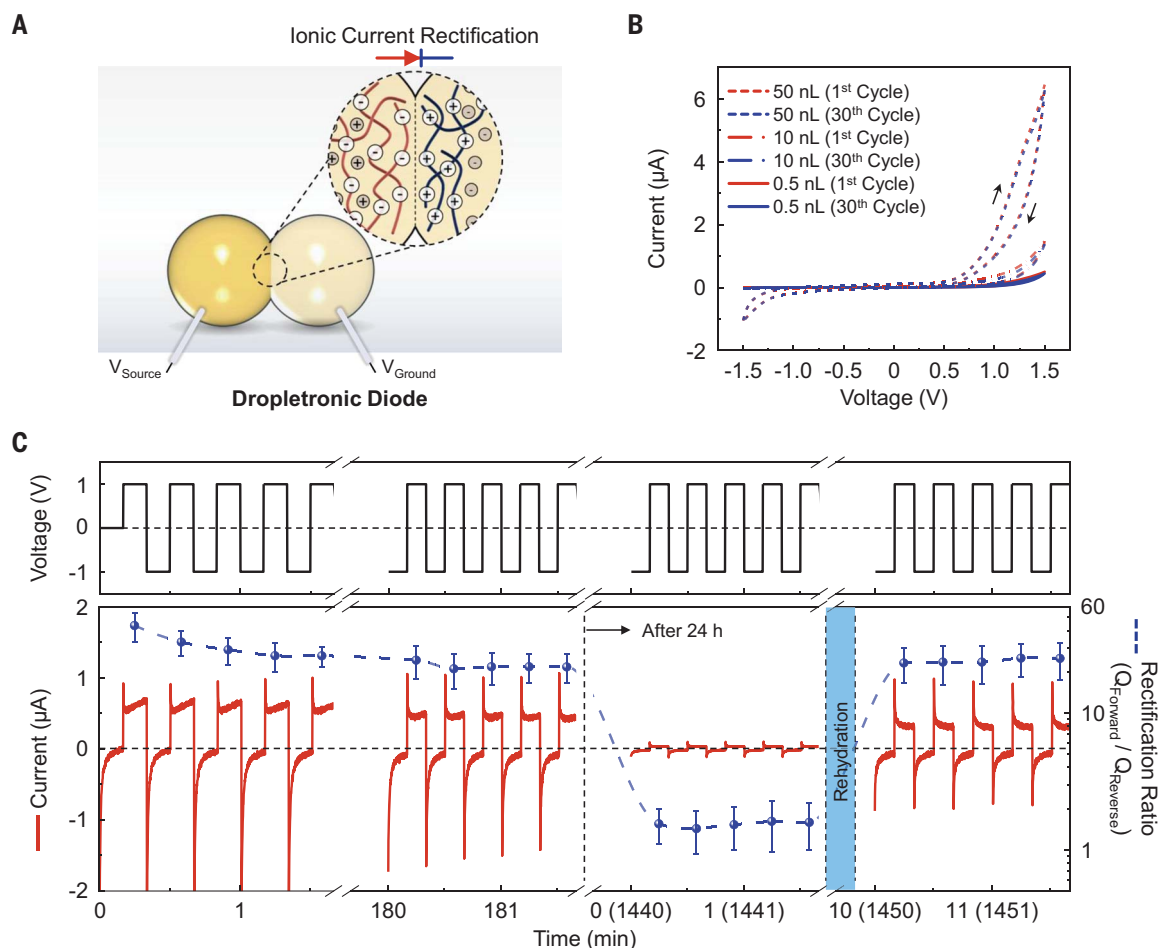


**Fig. 2. Ionic current rectification by dropletionic diodes.** (A) An ionic rectifying heterojunction was formed at the interface between the cation- and anion-selective hydrogel droplets. (B)  $I$ - $V$  curves of dropletionic diodes with droplet volumes of 50, 10, and 0.5 nL. Black arrows indicate the scan direction at a rate of  $100 \text{ mV s}^{-1}$ . (C) Rectification by dropletionic diodes under an alternating voltage of  $\pm 1 \text{ V}$  at  $0.05 \text{ Hz}$ . Droplet volume is  $0.5 \text{ nL}$ . The applied voltage is plotted on the top; the

current (red) and the charge rectification ratio (blue) are shown on the bottom, in which  $Q_{\text{Forward}}$  and  $Q_{\text{Reverse}}$  denote the total associated charges in one cycle under forward and reverse biases by integrating the current curve. Data were recorded for 3 hours under continuous operation after the UV cross-linking and for another 20 min after 24 hours, in which the droplets were soaked with water applied to the surface. Data in (B) and (C) are mean values  $\pm$  SD;  $n = 5$ .

the conductance of which depended on the salt concentration in the hydrogel, with  $100 \text{ mM}$  potassium chloride providing a high ionic conductance of  $51 \pm 18 \text{ nS}$  (module 1) and  $0.1 \text{ mM}$  potassium chloride a low ionic conductance of around  $4 \pm 1 \text{ nS}$  (module 2). The two NOT gates inverted input signals of  $0$  and  $1 \text{ V}$  with outputs of  $0.94$  and  $0.11 \text{ V}$  (module 1) and  $0.83$  and  $0.04 \text{ V}$  (module 2; Fig. 3G), representing the logical high of  $0.8$  to  $1 \text{ V}$  (logic value =  $1$ ) and the logical low of  $0$  to  $0.2 \text{ V}$  (logic value =  $0$ ). Moreover, connection of the two modules in series or in parallel produced an AND (Fig. 3H) or an OR gate (Fig. 3J), respectively. With the combination of two input voltages, different logic outputs were produced, consistent with the truth tables of the logic gates (Fig. 3, I and K). The AND and OR gates showed an information leakage of around  $8\%$  ( $0.92 \text{ V}$ ) and  $12\%$  ( $0.88 \text{ V}$ ) at the logical high, which are values comparable to those of the best solid-

state iontronic logic circuits (25, 27). The dropletionic logic circuits also exhibited fast-switching behavior between logical high and low, with a less than approximately  $5\text{-s}$  rise or fall time, which was more than  $10$  times faster than that of previous ionic logic circuits (25). By changing the circuit connections, NAND and NOR logic gates were also constructed (fig. S11). Dropletionic circuits may provide a route to build an ionic logic system for biomimetic information processing and computations.

#### Mimicking synaptic plasticity with dropletionics

Inspired by biological synapses (Fig. 4A), such as tripartite synapses that feature plasticity mediated through neurotransmitters and neuropeptides (34–36), we developed a synthetic synapse as an elaboration of the npn-type dropletionic transistor (a dropletionic transistor with ion memory; Fig. 4B). The device was constructed by attaching a conditioning drop-

let of untethered poly-L-lysine in native silk hydrogel to the base droplet of the transistor. We applied pulses of current to the conditioning droplet to drive the positively charged poly-L-lysine into or remove it from the base droplet, which contained negatively charged silk hydrogel. The poly-L-lysine thereby modulated the charge selectivity of the base droplet. The movement of the poly-L-lysine was reflected in the output characteristics ( $I_{\text{CE}}$ ) of the transistor (Fig. 4C), which displayed synaptic plasticity in terms of potentiation (i.e., an  $I_{\text{CE}}$  increase) and depression (i.e., an  $I_{\text{CE}}$  decrease). To assess the behavior of the synapse, we first applied a conditioning current ( $I_{\text{Con}}$ ) of  $+2$  or  $-2 \mu\text{A}$  for  $60 \text{ s}$ . The conditioning droplet was then switched off to an open-circuit mode ( $I_{\text{Con}} = 0 \mu\text{A}$ ), and after a delay of  $60 \text{ s}$ , the transistor output was read by stepping  $I_{\text{BE}}$  from  $0$  to  $0.5 \mu\text{A}$ , which had no noticeable impact on the synaptic weight (fig. S12). Potentiation and depression with  $I_{\text{Con}}$



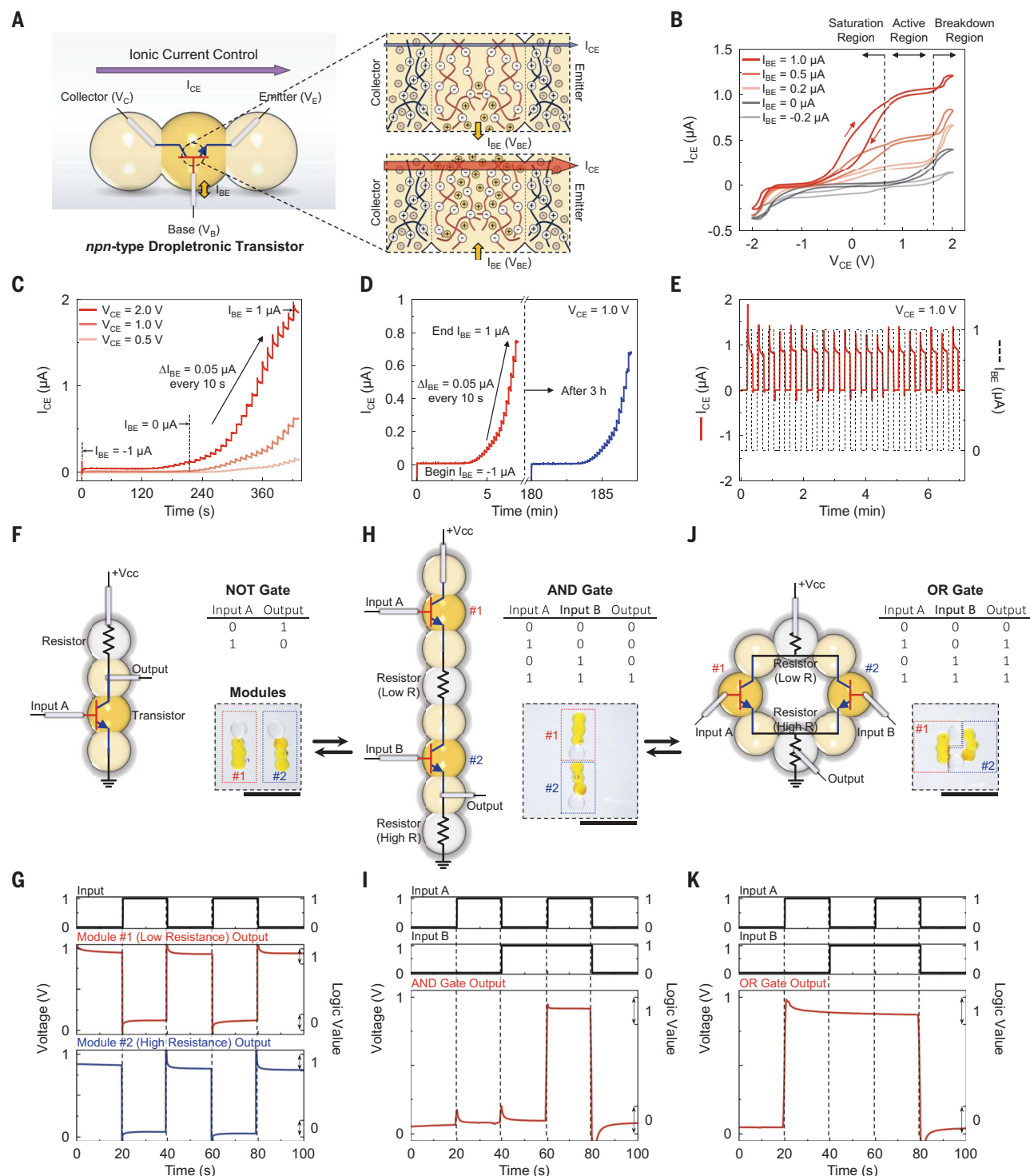


**Fig. 3. Dropletic transistor and reconfigurable logic gates.** (A) The npn-type transistor was formed by a droplet of cation-selective hydrogel sandwiched between two droplets of anion-selective hydrogel. The transistor was connected in a common-emitter configuration. The arrows indicate the current directions with anions as charge carriers of the output current (I<sub>CE</sub>) and cations as charge carriers of the input current (I<sub>BE</sub>). (B) Output characteristic (I<sub>CE</sub>-V<sub>CE</sub>) curves as a function of I<sub>BE</sub>, showing ion current saturation, active, and breakdown regions. Red arrows mark the scan direction at a rate of 50 mV s<sup>-1</sup>. (C) Response of I<sub>CE</sub> to stepwise increases

in I<sub>BE</sub> at 0.05 μA every 10 s from -1 to 1 μA. (D) Response of I<sub>CE</sub> before and after 3 hours of storage. (E) Off-on switching of I<sub>CE</sub> under an alternating I<sub>BE</sub> of 0 and 1 μA at 0.05 Hz. (F) Circuit diagram, truth table, and bright-field image of two dropletic NOT gates, which were used as modules to configure various two-input logic gates. (G) Output voltage of two NOT gates with a pulse train as input. (H to K) The AND gate (H) and OR gate (J) comprised the two NOT gates with different connections. The responses of the AND gate (I) and OR gate (K) to the four combinations of two inputs are shown. Droplet volume is 0.5 nl. Scale bars are 200 μm.

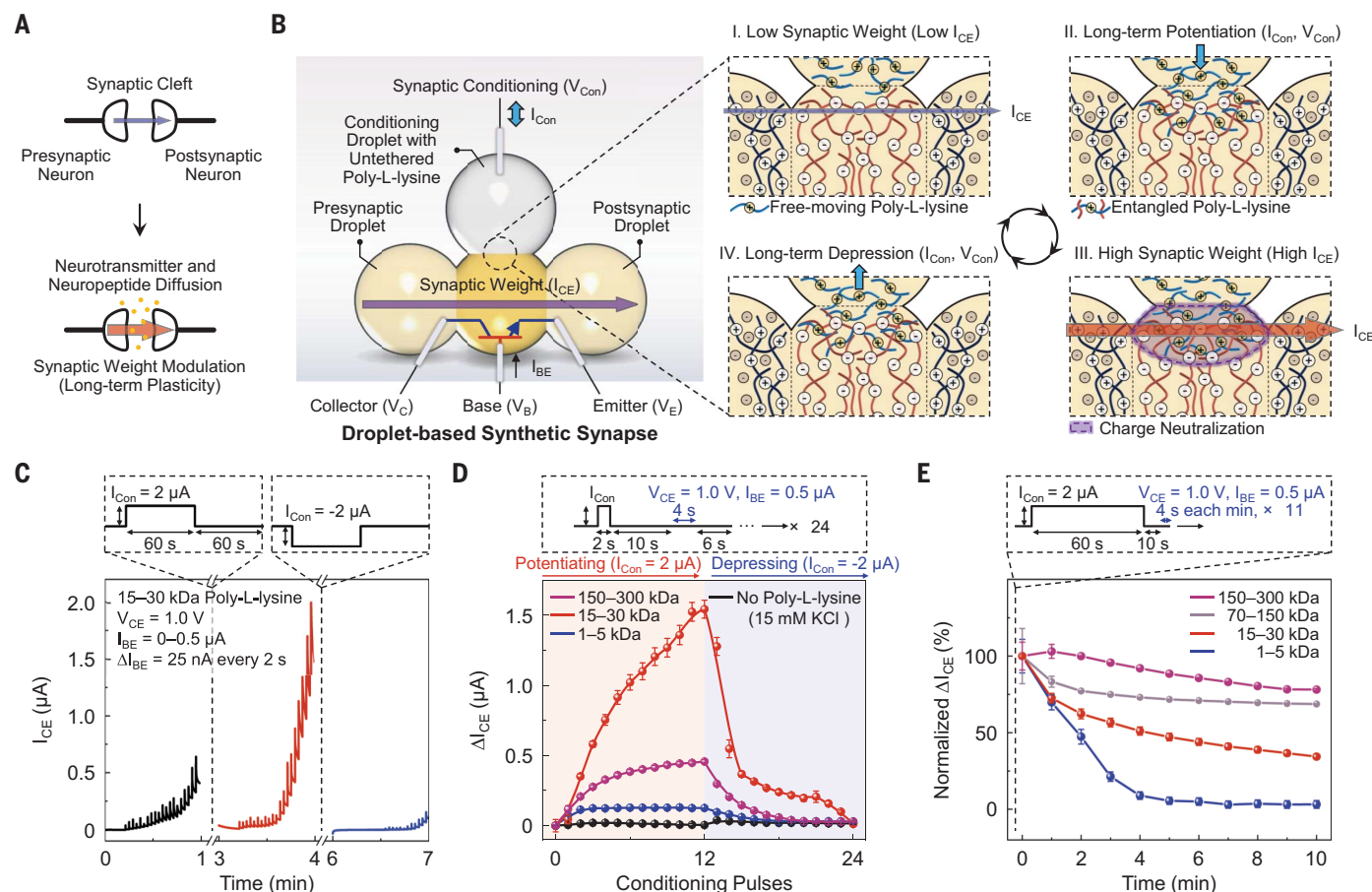


**Fig. 4. Droplet-based synthetic synapses.** (A) Biomolecular machinery in the synaptic cleft modulates the synaptic weight. (B) The synthetic synapse comprised an npn-type droplet transistor and one conditioning droplet connected to the base droplet. The collector, base, and emitter droplets mimicked the presynaptic neuron, the synaptic cleft, and the postsynaptic neuron, respectively. The conditioning droplet modulated the synaptic weight by delivering the contained poly-L-lysine into (from I to III) or retracting it from (from III to IV, then to I) the base droplet. The arrows indicate the current directions with anions as charge carriers of the output current ( $I_{CE}$ ) and cationic poly-L-lysine as charge carrier of the conditioning current ( $I_{con}$ ). (C) Output characteristics of the synthetic synapse

after applying a potentiating and a depressing  $I_{\text{Con}}$ . **(D)** Synaptic weight variations ( $\Delta I_{\text{CE}}$ ), with respect to the initial state, after consecutive potentiation and depression of the synthetic synapses with poly-L-lysine of different molecular weight ranges. Each conditioning contained a 2-s pulse of  $I_{\text{Con}} = +2$  or  $-2 \mu\text{A}$ , a 10-s delay, 4 s for synaptic weight measurement, and a 6-s interval. **(E)** Normalized  $\Delta I_{\text{CE}}$  after full potentiation, exhibiting long-term weight changes. Normalization was with respect to the initial state (0%) and potentiated state (100%) of each experiment. An  $I_{\text{Con}}$  of  $2 \mu\text{A}$  was applied for 60 s, followed by a 10-s delay, and then a 4-s synaptic weight measurement, which was repeated every minute. Droplet volume is 0.5 nl. Data in (D) and (E) are mean values  $\pm$  SD;  $n = 3$ .

led, respectively, to a fourfold increase and a threefold decrease in  $I_{CE}$  by comparison with the initial transistor output, demonstrating the role of poly-L-lysine in modulation of the synthetic synapse.

The long chain length and consequent slow diffusion of the poly-L-lysine confined within a silk fibroin network resulted in history-dependent memory, that is, long-term plasticity. We placed poly-L-lysine of various molecular weights in the conditioning droplet. Consecutive potentiating and depressing pulses enabled reversible modulation of the synaptic weight. An increase in the poly-L-lysine molecular weight from 1 to 5 kDa to 15 to 30 kDa increased the maximum change of synaptic weight ( $\Delta I_{CE}$ ) from 0.13 to 1.5  $\mu A$  after multiple conditioning pulses, whereas a further increase in molecular weight to 150 to 300 kDa reduced

$\Delta I_{\text{CE}}$  to around 0.45  $\mu\text{A}$  (Fig. 4D). These results might be attributed to a trade-off between the different total charges and diffusion dynamics of the poly-L-lysines. An extended poly-L-lysine chain provides a higher total charge but a decrease in diffusion rate, which would reduce the extent of insertion into the base droplet, thereby reducing the effect on synaptic weight. By contrast, replacing poly-L-lysine with potassium chloride in the conditioning droplet did not produce long-term synaptic plasticity because the potassium ions redistributed rapidly in hydrogels after initial modulation. By contrast, entanglement between poly-L-lysine chains and silk fibroins enabled prolonged ion memory in the range of minutes to hours. After an  $I_{\text{Con}}$  of 2  $\mu\text{A}$  for 60 s, which fully potentiated the synthetic synapse (fig. S13), the synaptic weight relaxed to a long-term value above its

initial state, showing an increased hysteresis with the increased poly-L-lysine molecular weight and thus chain length (Fig. 4E). Long-term plasticity, which can be modulated by ion size, has not been achieved with previous iontronic approaches (table S3) and offers an unconventional modulation pathway to neuromorphic applications.

## Dropletionics for electrophysiological recording

We examined the capability of dropletronics to interface with and record physiological activity in aqueous-based bioenvironments (Fig. 5A). An npn-type dropletronic transistor composed of 50-nl droplets was encapsulated in a thermoreversible organogel made from poly(styrene-*b*-ethylene-*co*-butylene-*b*-styrene) triblock copolymer to yield the portable dropletronic device. The organogel encapsulation

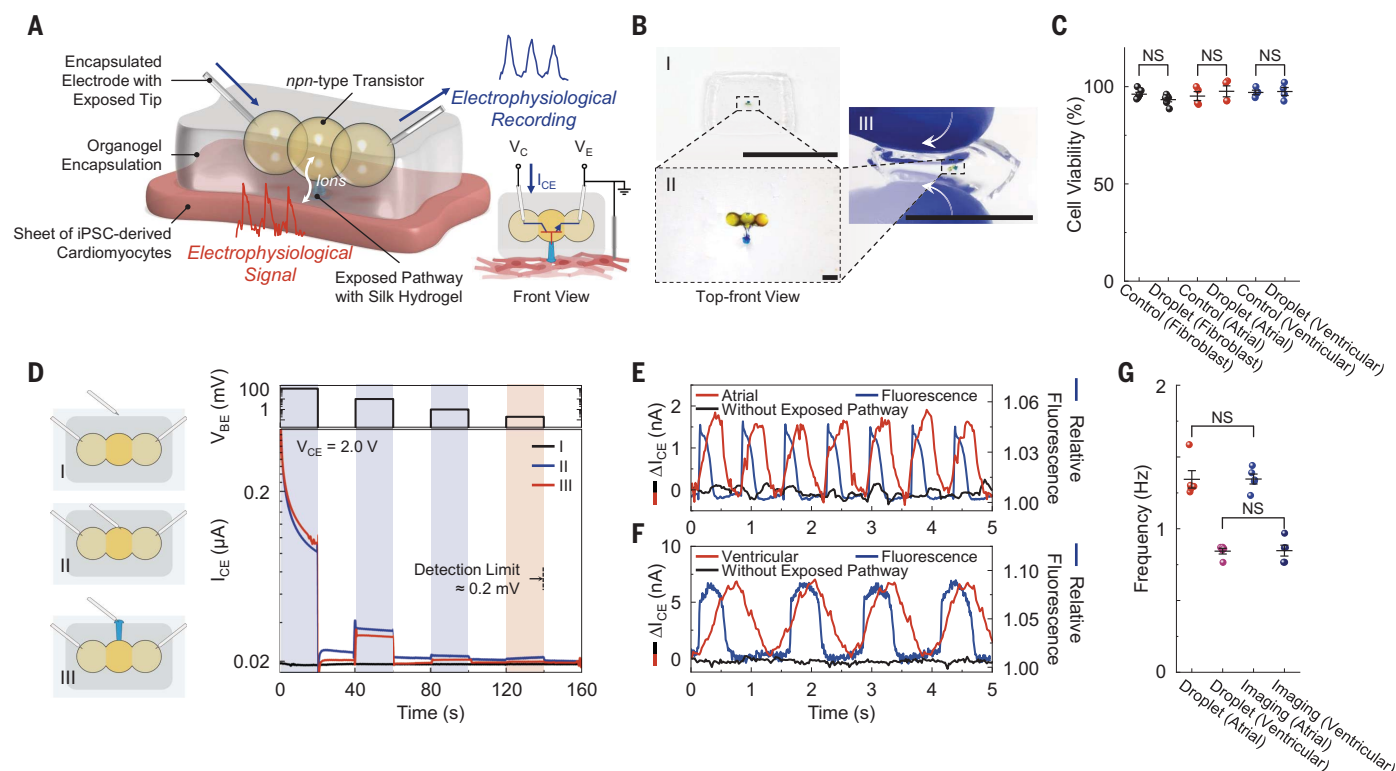


**Fig. 5. Electrophysiological recording by dropletionics.** (A) An organogel-encapsulated npn-type dropletionics transistor was interfaced with a tissue for electrophysiological recording. (B) Bright-field images of an encapsulated dropletionics device placed on a flat surface (I and II) and compressed and twisted by hand (III). Droplet volume is 50 nL. Scale bars are 1.5 cm (I and III) and 500  $\mu\text{m}$  (II). Blue food dye was used in the native silk hydrogel only for photography and was absent during the biological experiments. (C) Cell viability by live-dead staining of human fibroblasts or human iPSC-derived atrial and ventricular cardiomyocytes after attachment for 24 hours to the encapsulated dropletionics device. The control groups were not contacted with a dropletionics device. (D) Output currents ( $I_{CE}$ ) induced

by applying a silver chloride-coated silver electrode to deliver voltage pulses of 100, 10, 1, and 0.2 mV. Dropletionics devices were immersed in phosphate-buffered saline. Illustrations of different positions of the input electrode (I to III) are shown on the left (the blue component is the exposed pathway filled with the native silk hydrogel), and a plot of the data is shown on the right. (E and F) The dropletionics device output and fluorescence imaging of cell membrane potential from sheets of iPSC-derived atrial (E) and ventricular (F) cardiomyocytes. (G) Output fluctuation frequency of the dropletionics device versus the cardiac beating frequency measured by fluorescence imaging (control). NS indicates not significant; data were analyzed by two-sample *t* test. Data in (C) and (G) are mean values  $\pm$  SD;  $n = 5$ .

supported compression and twisting (Fig. 5B) and prevented the leakage of ions in physiological environments (7). By using cell viability assays (Fig. 5C) and MTT assays to test cell metabolic activity, the encapsulated dropletionics were shown to create no significant alteration to cell viability and to have good biocompatibility with human fibroblasts or cardiomyocytes derived from human induced pluripotent stem cells (iPSCs) (figs. S14 and S15). An exposed pathway with an inner diameter of around 300  $\mu\text{m}$  was created with a biopsy punch and filled with native silk hydrogel, which exposed the base droplet of the transistor to the external aqueous environment. When attached to a tissue surface, such as sheets of iPSC-derived atrial or ventricular cardiomyocytes, the electrophysiological signal from cellular activity acted as the  $I_{BE}$  and regulated ion transport in the dropletionics device (37, 38). To test the recording capability, we first applied a silver chloride-coated silver electrode to deliver voltage pulses as input signals (Fig. 5D). The device without

the exposed pathway had no response to input signals, whereas the dropletionics devices showed similar results when input pulses were applied to the proximal aqueous environment or directly applied to the base droplet by piercing through the soft encapsulation. The device was capable of recording input signals in the millivolt range with a detection limit of 0.2 mV (fig. S16).

Next, we placed the dropletionics device on sheets of iPSC-derived atrial or ventricular cardiomyocytes for recording electrophysiological signals of spontaneous cardiac activities. The traces exhibited signal-to-noise ratios of  $1.3 \pm 0.3$  and  $1.6 \pm 0.2$  dB for atrial (Fig. 5E) and ventricular cardiomyocytes, respectively (Fig. 5F) and remained stable for both cases for tens of minutes (fig. S17). No signal except noises from wired connections were measured without the exposed pathway, which excluded the mechanical interference from cardiac beating and therefore ensured that the recorded traces only documented electrophysiological signals. We observed a higher signal intensity ( $\Delta I_{CE}$ )

and a lower fluctuation frequency with the sheets of ventricular cardiomyocytes than with the atrial sheets, in agreement with the contraction characteristics of iPSC-derived cardiomyocytes (39, 40). Time-lapse fluorescence imaging of cell membrane potential revealed the spontaneous, periodic depolarization of the atrial and ventricular cardiomyocytes, which showed the same beating frequencies as recorded with the dropletionics device (Fig. 5G), indicating the device's validity.

## Conclusions

Until now, iontronics have been primarily manifested in solid-state systems of limited versatility (41–43). Further, miniaturization of iontronic solid-state systems is demanding and their biocompatibility is inadequate. In this work, a set of microscale, modular, soft, biocompatible dropletionics devices were self-assembled from freestanding nanoliter hydrogel droplets. Leveraging protein modifications, which conferred charge selectivity on silk hydrogels, allowed



the use of droplets with properties analogous to p- and n-type semiconductors. The hydrogel droplets enabled the fabrication of droplet-electronic diodes, transistors, reconfigurable logic gates, and synthetic synapses. Miniaturized droplet-electronics offers exceptional control of ion transport, fast temporal responses, and distinctive neuromorphic functionality, such as ionic polymer-mediated long-term plasticity. Given that cellular signaling uses ion transport, droplet-electronics can also act as a biocompatible interface between electronic and biological systems for sensing electrophysiological signals of cardiac activity, as demonstrated here.

Further advances will be required in order to develop more complex droplet-electronic circuits, for which microfluidics and three-dimensional droplet printers might offer fabrication solutions (44, 45). Realizing long lifetimes for droplet-electronic devices is a key goal, and the use of liquid-free ionoelastomers might help prolong ion conduction (23). To achieve complex logic functions with a cascade of droplet-electronic logic gates will require the optimization of droplet conductance and integration of additional droplet-electronic transistors to offset the output drift and reduce signal degradation (27). The accumulation of ion hysteresis and the associated increase in the system response time should also be considered when multiple droplet-electronic modules are integrated, for which further droplet miniaturization might provide a solution. Importantly, instead of droplet-electronics into a doomed competition with ultrahigh-performance silicon circuits, we envisage the integration of droplet-electronics with living matter (7, 46), which would provide a biocompatible means of direct ionic communication, including the possibility of simultaneously identifying multiple vital ionic species.

## REFERENCES AND NOTES

1. C. Wang et al., *Nat. Commun.* **8**, 15609 (2017).

2. Y. Dobashi et al., *Science* **376**, 502–507 (2022).
3. W. Chen et al., *Science* **382**, 559–565 (2023).
4. T. B. H. Schroeder et al., *Nature* **552**, 214–218 (2017).
5. K. Xiao et al., *Nat. Commun.* **10**, 74 (2019).
6. K. Xiao, L. Jiang, M. Antonietti, *Joule* **3**, 2364–2380 (2019).
7. Y. Zhang et al., *Nature* **620**, 1001–1006 (2023).
8. Y. Kim et al., *Science* **360**, 998–1003 (2018).
9. S. T. Keene et al., *Nat. Mater.* **19**, 969–973 (2020).
10. P. C. Harikeesh et al., *Nat. Commun.* **13**, 901 (2022).
11. T. Wang et al., *Nat. Electron.* **5**, 586–595 (2022).
12. T. Sarkar et al., *Nat. Electron.* **5**, 774–783 (2022).
13. P. Robin et al., *Science* **379**, 161–167 (2023).
14. T. Xiong et al., *Science* **379**, 156–161 (2023).
15. S. H. Han, S. I. Kim, M.-A. Oh, T. D. Chung, *Proc. Natl. Acad. Sci. U.S.A.* **120**, e2211442120 (2023).
16. Z. Lei, P. Wu, *Matter* **6**, 429–444 (2023).
17. C. Yang, Z. Suo, *Nat. Rev. Mater.* **3**, 125–142 (2018).
18. O. J. Cayre, S. T. Chang, O. D. Velez, *J. Am. Chem. Soc.* **129**, 10801–10806 (2007).
19. S.-M. Lim et al., *Proc. Natl. Acad. Sci. U.S.A.* **116**, 13807–13815 (2019).
20. H. R. Lee et al., *Adv. Funct. Mater.* **29**, 1806909 (2019).
21. K. Tybrandt, K. C. Larsson, A. Richter-Dahlfors, M. Berggren, *Proc. Natl. Acad. Sci. U.S.A.* **107**, 9929–9932 (2010).
22. K. Tybrandt, E. O. Gabrielson, M. Berggren, *J. Am. Chem. Soc.* **133**, 10141–10145 (2011).
23. H. J. Kim, B. Chen, Z. Suo, R. C. Hayward, *Science* **367**, 773–776 (2020).
24. Y. Xue et al., *Science* **372**, 501–503 (2021).
25. K. Tybrandt, R. Forchheimer, M. Berggren, *Nat. Commun.* **3**, 871 (2012).
26. E. O. Gabrielson, P. Janson, K. Tybrandt, D. T. Simon, M. Berggren, *Adv. Mater.* **26**, 5143–5147 (2014).
27. B. Sabbagh, N. E. Fraiman, A. Fish, G. Yossifon, *ACS Appl. Mater. Interfaces* **15**, 23361–23370 (2023).
28. L. Bocquet, *Nat. Mater.* **19**, 254–256 (2020).
29. J. K. Sahoo, O. Hasturk, T. Falcucci, D. L. Kaplan, *Nat. Rev. Chem.* **7**, 302–318 (2023).
30. Z. Lin et al., *ACS Nano* **15**, 5649–5660 (2021).
31. Y. Zhang et al., *Nat. Chem. Eng.* 10.1038/s44286-024-00136-z (2024).
32. X. Cui et al., *Adv. Healthc. Mater.* **9**, 1901667 (2020).
33. B. G. Streetman, S. Banerjee, *Solid State Electronic Devices* (Pearson, ed. 7, 2015).
34. M. Arizono et al., *Nat. Commun.* **11**, 1906 (2020).
35. F. Randi, A. K. Sharma, S. Dvali, A. M. Leifer, *Nature* **623**, 406–414 (2023).
36. H. Wang et al., *Science* **382**, eabq8173 (2023).
37. N. Li et al., *Science* **381**, 686–693 (2023).
38. P. Li et al., *Science* **384**, 557–563 (2024).
39. M. Kleinsorge, L. Cyganek, *STAR Protoc.* **1**, 100026 (2020).
40. P. Robinson et al., *J. Mol. Cell. Cardiol.* **180**, 44–57 (2023).
41. K. Xiao, C. Wan, L. Jiang, X. Chen, M. Antonietti, *Adv. Mater.* **32**, e2000218 (2020).
42. J. Zhang, W. Liu, J. Dai, K. Xiao, *Adv. Sci. (Weinh.)* **9**, e2200534 (2022).
43. P. Robin, L. Bocquet, *J. Chem. Phys.* **158**, 160901 (2023).
44. G. Villar, A. D. Graham, H. Bayley, *Science* **340**, 48–52 (2013).
45. S. Bachler, D. Haidas, M. Ort, T. A. Duncombe, P. S. Dittrich, *Commun. Biol.* **3**, 769 (2020).
46. Y. Jin et al., *Nat. Commun.* **14**, 5986 (2023).
47. Y. Zhang, C. M. J. Tan, C. N. Toeffer, X. Lu, H. Bayley, Data for: Microscale droplet assembly enables biocompatible multifunctional modular iontronics, Version 1. Zenodo (2024); <https://doi.org/10.5281/zenodo.13378258>.

## ACKNOWLEDGMENTS

We thank X. Wang (Bayley Group, University of Oxford) for helpful discussions. We acknowledge the use of KOLF 2.1J iPSCs in this research. The parental cell line from which the iPSCs were generated was produced by the Sanger Institute as part of the Human-iPSC Initiative. The National Institutes of Health (NIH) and the NIH's iPSC Neurodegenerative Disease Initiative supported the iPSC generation. **Funding:** This work was supported by the John Fell Oxford University Press Research Fund (grants 0011303 and 0013171), a European Research Council Advanced Grant (SYNTISU), European Research Council Proof of Concept grants (BIOELECTRIC and SYMPLANT), a Wellcome Sir Henry Dale Fellowship (222567/Z/21/Z), and grants from the Oxford Martin School and the Ludwig Institute for Cancer Research. **Author contributions:** Y.Z. conceived the ideas. Y.Z. designed, performed, and analyzed the experiments. C.M.J.T., C.N.T., and X.L. assisted with the iPSC-derived cardiomyocyte experiments and biocompatibility tests. C.M.J.T. assisted with the interpretation and analysis of the cell experiments. Y.Z. and H.B. discussed the data and wrote the paper. All authors discussed the results and commented on the manuscript. **Competing interests:** Y.Z. and H.B. are inventors on a patent application filed through Oxford University Innovation. The other authors declare no competing interests. **Data and materials availability:** All data needed to evaluate the conclusions in the paper are present in the paper or the supplementary materials. The data that support the findings of this study are available at Zenodo (47). **License information:** Copyright © 2024 the authors, some rights reserved; exclusive licensee American Association for the Advancement of Science. No claim to original US government works. <https://www.science.org/about/science-licenses-journal-article-reuse>

## SUPPLEMENTARY MATERIALS

[science.org/doi/10.1126/science.adr0428](https://science.org/doi/10.1126/science.adr0428)

Materials and Methods

Supplementary Text

Figs. S1 to S17

Tables S1 to S3

References (48–83)

Submitted 14 June 2024; accepted 4 October 2024  
10.1126/science.adr0428